

Contents lists available at ScienceDirect

Acta Astronautica

journal homepage: www.elsevier.com/locate/actaastro





Inertia tensor estimation of tethered debris through tether tracking

Derek Bourabah, Chris Gnam, Eleonora M. Botta*

Department of Mechanical and Aerospace Engineering, University at Buffalo, Buffalo, NY, United States

ARTICLE INFO

Keywords: Unscented Kalman filter Space debris Moments of inertia Estimation Tethered capture Camera model

ABSTRACT

Tethered systems, such as tethered harpoons or nets, are promising methods to capture uncooperative space debris, but suffer from complicated post-capture dynamics and control; control strategies could benefit from knowledge of the mass moments of inertia of the target debris, usually unknown without estimation. In this work, an Unscented Kalman Filter is proposed to estimate the moments of inertia, angular velocity, and attitude of tethered debris in the absence of end effectors and of sensors on the target. This is achieved by leveraging camera measurements of features on the target debris and a tension sensor. Estimation of the properties of (1) a symmetric target with a centered tether attachment point and of (2) a non-symmetric target with a noncentered tether attachment point is performed in simulation. The filter is found to be capable of accurately and precisely estimating both the attitude and angular rates of debris, although sustained loss of a tracked feature heavily impairs these estimates. The principal moments of inertia estimates are unaffected by the loss of a tracked feature and can be made both accurately and precisely when the tether is taut. Asymmetry of the target and of the tether attachment point can have a positive effect on the performance of the filter.

1. Introduction

The necessity of removing the largest and more massive pieces of debris from low-earth orbit has been made clear by multiple collisions and an increased space junk density [1-3]. Numerous space debris removal methods have been proposed to clean the space environment. Among the considered debris removal strategies, two methods of particular interest are tethered nets [4-8] and harpoons [9-11], where the debris is captured and connected to the chaser spacecraft via a tether. Tether-based methods of capture are characterized by increased safety over traditional methods of debris capture, such as robotic arms, since they allow the chaser to maintain a larger distance from the target. However, tether-based capture introduces additional challenges. As the physical connection between the target and chaser is a tether, which is flexible and cannot withstand compression, control of the target is both particularly important and difficult. Post-capture control is complicated by the fact that debris is uncooperative and unresponsive, and its properties are largely unknown. Moreover, the coupled target and chaser dynamics can introduce chaotic motion [12,13], further complicating control of the tethered system. Control of the attitude motion of the debris has been studied by several authors [14-18] and would help mitigate the onset of chaos. The proposed methods, however, can be improved if the moment of inertia parameters of the debris - otherwise unknown - could be determined. In fact, knowing the moments of inertia provides the ability to estimate how the target debris will rotate and react to different control inputs.

To estimate the moments of inertia of the target, there must be a determinable moment affecting the target, or else only the ratios of the principal moments of inertia may be found [19,20]. Often, only the ratios are found prior to debris capture, when the debris is freely rotating [21,22]. However, robotic capture of debris allows estimation of all moment of inertia parameters due to the rigid connection between the target and chaser spacecraft [23-28]. Although some estimation for tethered satellite systems has been performed (i.e., for the tether's curvature [29,30]), work on the estimation of the individual principal moments of inertia following the capture of space debris via a tether is scarce. Zhang et al. achieved estimation of the difference between two principal moments of inertia, and of the value of one principal moment of inertia of a tethered target [31]. In previous work, Bourabah et al. showed that it is possible to obtain precise and accurate estimates of the principal moments of inertia of tethered debris when perfect knowledge of the tension in the tether and angular rate measurements of the target debris are available [32]. The performance of two Extended Kalman Filters and of an Unscented Kalman Filter (UKF) was also compared, and it was found that improvements from the UKF were significant [32].

In this work, numerous assumptions are relaxed from our prior work, in which angular rate measurements were required: Instead of assuming that direct measurements of the angular velocity of a tethered target are available – which would mean that a gyroscope on the target is able to provide information to the chaser spacecraft – pixel

E-mail addresses: derekbou@buffalo.edu (D. Bourabah), crgnam@buffalo.edu (C. Gnam), ebotta@buffalo.edu (E.M. Botta).

^{*} Corresponding author.

measurements are simulated to mimic feature (or landmark) tracking of the target debris via a camera on the chaser spacecraft. In releasing this assumption, the tether may truly be passive with no manipulator at the end to provide measurements to the chaser, or thrust on the target. Here, the only available force for estimation is the tension force in the tether, which can be measured at the chaser's side. Moreover, the assumption that tension in the tether is perfectly known is relaxed by considering that the tension in the tether is measured and affected by sensor noise. By estimating the tension vector and the attitude of the target, the torque applied on the debris by the tension force can be estimated, which in turn allows for estimating the principal moments of inertia.

A combined UKF and Unscented Quaternion Estimator (USQUE) formulation is applied to tethered debris systems for the first time, to estimate the attitude, angular rates, and principal moments of inertia of the tethered target. The proposed estimation methodology is applied to two test cases: (1) a symmetric target with a centered tether attachment point and (2) a non-symmetric target with a non-centered tether attachment point. The results of estimation demonstrate that tracking two points via a camera and employing a single tension sensor allows estimating the principal moments of inertia of tethered debris both accurately and precisely, in both the simulated cases. Therefore, no additional hardware to attach sensors on the target or to impart a known torque or force on the debris is required to estimate the principal moments of inertia. It is also demonstrated that asymmetry of the target and of the tether attachment point can have a positive effect on the performance of the filter.

The rest of this paper is organized as follows. Section 2 discusses the system model and dynamics of the chaser–tether–target system, and the UKF methodology is explained in Section 3. Section 4 details the generation of synthetic measurements and the estimation results of the UKF in the case of a symmetric target with a centered tether attachment point, whereas Section 5 reports the main estimation results for the case of a non-symmetric target with a non-centered tether attachment point. Finally, the conclusions of the work are provided in Section 6.

2. System dynamics

The system under consideration consists of a chaser spacecraft and target debris connected by a single tether (see Fig. 1). In this work, the chaser spacecraft and target debris are modeled as rigid bodies, whereas the tether is modeled as a single Kelvin–Voigt viscoelastic element, non-linearized to represent the inability of the tether to withstand compression. In Fig. 1, the Earth-Centered Inertial (ECI) reference frame is represented by frame \mathcal{O} , whereas the chaser and target body frames are marked as \mathcal{C} and \mathcal{T} , respectively. The position vectors of the tether attachment point on the chaser and target in their respective body frames are indicated with $r_{tp,C}$ and $r_{tp,T}$. The unit vector \hat{e} denotes the direction of the tether – from the target to the chaser – and the vectors \mathbf{R}_C and \mathbf{R}_T denote the chaser's and target's center of mass positions in the ECI frame.

Although the complete dynamic formulation for this system can be found in previous work [32], key equations for the simulation of the dynamics of the system are reported here for the sake of completeness. The attitude dynamics and kinematics of the chaser and target are given by Eq. $(1)^1$:

$$\dot{\mathbf{q}} = \frac{1}{2} \begin{bmatrix} I_{3\times3} q_4 + S(q_v) \\ -q_v^T \end{bmatrix} \boldsymbol{\omega}$$
 (1a)

$$\dot{\boldsymbol{\omega}} = \boldsymbol{J}^{-1} \left(\boldsymbol{\tau} + \boldsymbol{r}_{tp} \times (^{\mathcal{X}} \boldsymbol{A}^{\mathcal{O}} \boldsymbol{T}) - \boldsymbol{\omega} \times \boldsymbol{J} \boldsymbol{\omega} \right) \tag{1b}$$

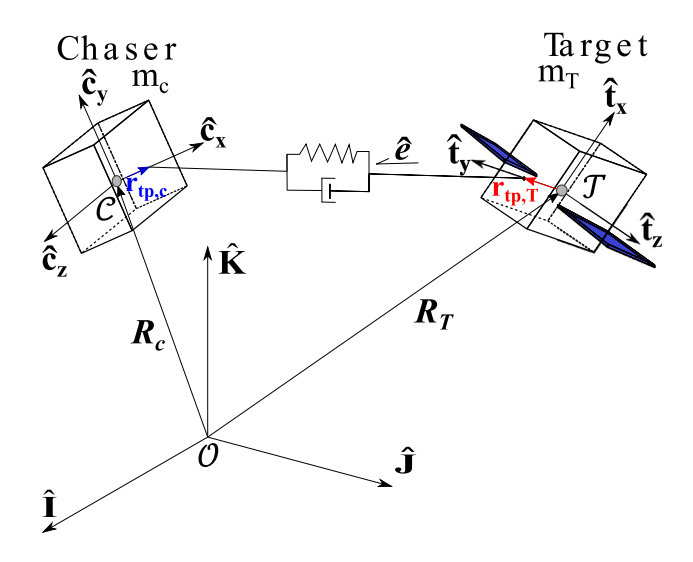


Fig. 1. System model with reference frames and notable vectors.

where q is the quaternion representation of the attitude of the chaser or target and ω is the angular velocity vector. The quaternion array follows $q = [q_v^T, q_4]^T$, where $q_v = [q_1, q_2, q_3]^T$ is the vector component and q_4 is the scalar component. The operator S(*) denotes the skewsymmetric matrix (i.e., the cross-product matrix) with components of *, and I is an identity matrix. In the angular rate dynamics, the moment of inertia matrix is denoted with J, the tether attachment point is given by r_{tp} , and the symbol τ represents all external moments on the body other than the moment generated by the tension force. In this work, the only external moments affecting the system are those generated by the control forces on the chaser craft, and there are no external moments affecting the target debris other than the moment generated by the tension force. Vector T denotes the tension vector in the ECI frame, whereas ${}^{\mathcal{X}}A^{\mathcal{O}}$ is a rotation matrix transforming a vector from frame \mathcal{O} to frame \mathcal{X} , where \mathcal{X} represents the target or chaser body frame.

In accordance with the non-linearized visco-elastic tether model, the magnitude of the tension force is calculated using $T = \max(k(l-l_0) + c\dot{l}, 0)$, where the natural tether length is denoted by l_0 , the current tether length is denoted by l_1 , and l_1 denotes the relative speed of the tether attachment point on the target with respect to the tether attachment point on the chaser in the tether direction, \hat{e} . The stiffness and damping coefficients of the tether are given by k and c, respectively. The tension vector can then be calculated in the inertial frame with $T = T\hat{e}$ for the target and $T = -T\hat{e}$ for the chaser.

3. Unscented Kalman filtering

To estimate the inertial parameters of the target using simulated pixel and tension measurements, a UKF is implemented. Among the existing filtering techniques, the UKF is selected due to the nonlinear dynamics of the system and its proven performance in previous work [32]. The implementation of the UKF is standard for the moment of inertia and angular rate estimates. However, the attitude component of the filter follows an USQUE formulation as was presented by Crassidis and Markley [33,34]. For the reader's convenience, the main steps are covered in the remainder of this Section.

3.1. Dynamics model

The UKF uses a finite set of deterministically selected samples, known as sigma points, to represent a Gaussian distribution. If the

 $^{^{1}}$ Here, subscripts for the target and chaser are omitted for the sake of simplicity. With the exception of the tension vector T, all variables are in the corresponding body-fixed frame.

covariance matrix P_k at the kth estimate has dimension $n \times n$, where n is the number of estimated states, a matrix of sigma points (χ_k) is generated by taking the columns of the $n \times 2n$ matrix $\sigma_k = \pm \sqrt{(n+\lambda)P_k}$. Here, the matrix square root is obtained through Cholesky decomposition, $\lambda = \alpha^2(n+\kappa) - n$ is a scaling parameter, and α and κ are tuning parameters, where α controls the spread of the sigma point distribution, while κ is used to fine-tune higher-order moments [35].

In this work, the states are given by three Euler error angles $\delta p = [\delta p_x, \delta p_y, \delta p_z]^T$ about the roll, pitch, and yaw axes, three corresponding angular rates $\boldsymbol{\omega} = [\omega_x, \omega_y, \omega_z]^T$, and three principal moments of inertia parameters $\boldsymbol{J} = [J_x, J_y, J_z]^T$ for the target debris. While not a state, an initially estimated quaternion attitude representation of the target, \hat{q}_0 , must also be provided to the filter.

If μ_k is the mean of the distribution representing the estimated states at the kth iteration, then the sigma points are

$$\chi_k(i) = \begin{cases} \boldsymbol{\mu}_k = [\hat{\boldsymbol{\delta}} \hat{\boldsymbol{p}}_k^T, \hat{\boldsymbol{\phi}}_k^T, \hat{\boldsymbol{J}}_k^T]^T & \text{for } i = 0\\ \sigma_k(i) + \boldsymbol{\mu}_k & \text{for } i = 1, 2, \dots, 2n \end{cases}$$
 (2)

where (i) denotes the ith column of a matrix. The sigma points are separated into three sections of three parameters according to $\chi_k = \chi_k(i) = [(\chi_k^{\delta p})^T, (\chi_k^{\omega})^T, (\chi_k^J)^T]^T$. A matrix of quaternions, \hat{q}_k , is then generated using the Euler error components of the kth χ_k points, $\chi_k^{\delta p}$, through the corresponding error quaternion $\delta q_k(i)$, as:

$$\hat{q}_k = \hat{q}_k(i) = \delta q_k(i) \otimes \hat{q}_k(0) \tag{3}$$

where \otimes indicates the quaternion product and

$$\delta q_{k}(i) = \begin{bmatrix} \delta \varrho_{k}(i) \\ \delta q_{4_{k}}(i) \end{bmatrix} = \begin{bmatrix} \left(a + \delta q_{4_{k}}(i) \right) \chi_{k}^{\delta p} / \phi \\ \frac{-a \|\chi_{k}^{\delta p}\|^{2} + \phi \sqrt{\phi^{2} + (1 - a^{2})} \|\chi_{k}^{\delta p}\|^{2}}{\phi^{2} + \|\chi_{k}^{\delta p}\|^{2}} \end{bmatrix}$$
(4)

where a is a number between 0 and 1, ϕ is calculated as 2(a+1), and the first column of the quaternion matrix, $\hat{q}_k(0)$, is set to the kth mean estimated quaternion. In this work, a is selected to be 1. The modified sigma points in the UKF are now given as $\chi_{k,m} = \chi_{k,m}(i) = [\hat{q}_k^T, (\chi_k^\omega)^T, (\chi_k^J)^T]^T$. These modified sigma points are propagated through the system dynamics, converted back to the original sigma points, and then weighted to give the propagated mean and covariance:

$$\hat{\mathbf{x}}_{k+1}^{-} = \sum_{i=0}^{2n} W_i^{\text{mean}} \chi_{k+1}(i)$$
 (5a)

$$P_{k+1}^{-} = \sum_{i=0}^{2n} W_i^{\text{cov}} \Psi \Psi^T + Q_{k+1}$$
 (5b)

where $\Psi \equiv \chi_{k+1}(i) - \hat{\mathbf{x}}_{k+1}^-$, Q_{k+1} is the discrete-time process noise covariance –which takes into account uncertainties in the dynamics and modeling errors–, and W_i^{mean} and W_i^{cov} are the weights for the ith sigma point, given by:

$$W_0^{\text{mean}} = \frac{\lambda}{n+\lambda} \tag{6a}$$

$$W_0^{\text{cov}} = \frac{\lambda}{n+\lambda} + (1 - \alpha^2 + \beta)$$
 (6b)

$$W_i^{\text{mean}} = W_i^{\text{cov}} = \frac{1}{2(n+\lambda)}, \quad i = 1, 2, ..., 2n$$
 (6c)

where β becomes the third tuning parameter and is used to incorporate prior knowledge of the distribution [35].

The dynamics for each $\chi_{k,m}$ point in the UKF is propagated using a Runge–Kutta 4th order integrator and follows:

$$\dot{\chi}_{m} = \begin{bmatrix} \dot{q}_{1} \\ \dot{q}_{2} \\ \dot{q}_{3} \\ \dot{q}_{4} \\ \dot{\phi}_{x} \\ \dot{\phi}_{y} \\ \dot{\phi}_{z} \\ \dot{f}_{y} \\ \dot{f}_{z} \end{bmatrix} = \begin{bmatrix} (\hat{q}_{4}\hat{\omega}_{x} - \hat{q}_{3}\hat{\omega}_{y} + \hat{q}_{2}\hat{\omega}_{z})/2 \\ (\hat{q}_{3}\hat{\omega}_{x} + \hat{q}_{4}\hat{\omega}_{y} - \hat{q}_{1}\hat{\omega}_{z})/2 \\ (\hat{q}_{1}\hat{\omega}_{y} - \hat{q}_{2}\hat{\omega}_{x} + \hat{q}_{4}\hat{\omega}_{z})/2 \\ (-\hat{q}_{1}\hat{\omega}_{x} - \hat{q}_{2}\hat{\omega}_{y} - \hat{q}_{3}\hat{\omega}_{z})/2 \\ (r_{y}\hat{T}_{z} - r_{z}\hat{T}_{y} - \hat{\omega}_{y}\hat{J}_{z}\hat{\omega}_{z} + \hat{\omega}_{z}\hat{J}_{y}\hat{\omega}_{y})/\hat{J}_{x} \\ (r_{z}\hat{T}_{x} - r_{x}\hat{T}_{z} - \hat{\omega}_{z}\hat{J}_{x}\hat{\omega}_{x} + \hat{\omega}_{x}\hat{J}_{z}\hat{\omega}_{z})/\hat{J}_{y} \\ (r_{x}\hat{T}_{y} - r_{y}\hat{T}_{x} - \hat{\omega}_{x}\hat{J}_{y}\hat{\omega}_{y} + \hat{\omega}_{y}\hat{J}_{x}\hat{\omega}_{x})/\hat{J}_{z} \\ 0 \\ 0 \end{bmatrix}$$

$$(7)$$

where r_x , r_y , and r_z are used to represent the corresponding components of the position of the tether attachment point on the target debris in the target body frame (i.e., ${}^Tr_{tp,T}$). As the individual components of the tension are not measured and are instead based on the estimated attitude of the target debris, the tension components are denoted by a caret (i.e., \hat{T}_x , \hat{T}_y , and \hat{T}_z). To obtain the estimated tension components, the tension unit vector is created using the relative position of the satellites and the positions of the tether attachment points on the corresponding spacecraft or debris following:

$$\hat{\boldsymbol{e}} = \left(\boldsymbol{R}_C + {}^{\mathcal{O}}\boldsymbol{A}^{CC}\boldsymbol{r}_{tp,C}\right) - \left(\boldsymbol{R}_T + {}^{\mathcal{O}}\boldsymbol{A}^{TT}\boldsymbol{r}_{tp,T}\right)$$

$$\hat{\boldsymbol{T}} = {}^{\mathcal{T}}\boldsymbol{A}^{\mathcal{O}}\tilde{\boldsymbol{T}}\hat{\boldsymbol{e}}$$
(8)

where ${}^{\mathcal{T}}A^{\mathcal{O}}$ and ${}^{\mathcal{O}}A^{\mathcal{T}}$ are created using the estimated attitude quaternion of the target debris. The inertial positions and respective body frame tether attachment points of the chaser and target are assumed to be known (i.e., R_C , R_T , $r_{tp,C}$, and $r_{tp,T}$), whereas the tension magnitude, \tilde{T} , is measured.

The propagated points are now given by $\chi_{k+1,m} = [\hat{q}_{k+1}^T, (\chi_{k+1}^\omega)^T, (\chi_{k+1}^J)^T]^T$. To recover the unmodified χ_{k+1} points in terms of the error angle representation, each quaternion must be converted back to $\chi_{k+1}^{\delta p}$ (i.e., the quaternions are converted back to Euler error angles) by:

$$\chi_{k+1}^{\delta p}(i) = \begin{cases} \mathbf{0} & \text{if } i = 0\\ \frac{\phi \delta \varrho_{k+1}(i)}{a + \delta q_{4_{k+1}}(i)} & \text{if } i = 1, 2, \dots, 2n \end{cases}$$
(9)

where $\delta \varrho_{k+1}(i)$ and $\delta q_{4_{k+1}}(i)$ are given by:

$$\delta q_{k+1} = \delta q_{k+1}(i) = \begin{bmatrix} \delta \varrho_{k+1}(i) \\ \delta q_{4_{k+1}}(i) \end{bmatrix} = \hat{q}_{k+1}(i) \otimes \hat{q}_{k+1}(0) \tag{10}$$

Using the restored sigma points, $\chi_{k+1} = [(\chi_{k+1}^{\delta p})^T, (\chi_{k+1}^{\omega})^T, (\chi_{k+1}^J)^T]^T]^T$, the mean estimates can be found (through Eq. (5)) and updated using measurements. For this work, it is assumed that two points on the target are being tracked, with the first being the tether attachment point on the target debris and the second being a randomly selected point on the debris whose body-fixed position on the target debris is assumed to be known. Measurements of these points are assumed to come from a pinhole projection model of a camera. It is further assumed that these points are never hidden from the camera by the geometry of the target. It should be noted that, in reality, the optical tracking of these features will require image processing. However, image processing algorithms are beyond the scope of this work; instead, it is assumed here that the detection and matching of features is done as a pre-processing step and that the resulting pixel measurements are fed directly to the filter.

3.2. Measurement model

At discrete observation times, the states are updated with the information contributed by the measurement. Measurements are of the form:

$$\tilde{\mathbf{y}}_k = \mathbf{h}(\mathbf{x}_k) + \mathbf{v}_k \tag{11}$$

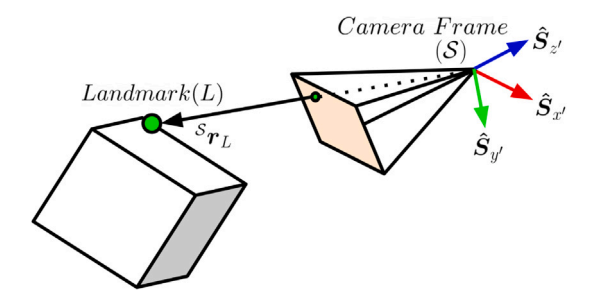


Fig. 2. Geometry of the camera measurement model.

where $\tilde{\mathbf{y}}_k$ is the measurement vector and \mathbf{v}_k is the measurement noise, which is assumed to be a vector of zero-mean Gaussian random variables with covariance \mathbf{R}_k . The predicted measurement for each sigma point is computed as:

$$\gamma_{k+1}(i) = \mathbf{h}(\chi_{k+1}(i)) \tag{12}$$

The specific pinhole projection model used for pixel coordinate measurements can be written as:

$$\gamma_{k+1}(i) = \begin{bmatrix} d_{x'} \\ d_{y'} \end{bmatrix} = \begin{bmatrix} c_{x'} - s_{x'} \left(\frac{\epsilon_1}{\epsilon_3}\right) \\ c_{y'} + s_{y'} \left(\frac{\epsilon_2}{\epsilon_3}\right) \end{bmatrix}$$
(13)

where $d_{x'}$ and $d_{y'}$ are pixel coordinates in the image, $c_{x'}$ and $c_{y'}$ are the x'- and y'- pixel coordinates of the center of the image, $s_{x'}$ and $s_{y'}$ are the scales between the image space and the world space – calculated by dividing the image resolution by the sensor size – and ϵ is given by:

$$\epsilon = \begin{bmatrix} \epsilon_1 \\ \epsilon_2 \\ \epsilon_3 \end{bmatrix} = \begin{bmatrix} f & 0 & 0 \\ 0 & f & 0 \\ 0 & 0 & 1 \end{bmatrix} \cdot {}^{S}\mathbf{r}_{L} \tag{14}$$

where f is the focal length of the camera, and ${}^{S}r_{L}$ is the position of a landmark L in the *camera* frame, S. A diagram of this frame is shown in Fig. 2.

3.3. Estimate update

To update the predicted states, the output covariance matrix P_{k+1}^{yy} and the cross-correlation matrix P_{k+1}^{xy} are first found as:

$$P_{k+1}^{yy} = \sum_{i=0}^{2n} W_i^{\text{cov}} \left[\gamma_{k+1}(i) - \hat{\mathbf{y}}_{k+1}^- \right] \left[\gamma_{k+1}(i) - \hat{\mathbf{y}}_{k+1}^- \right]^T$$
 (15a)

$$P_{k+1}^{xy} = \sum_{i=0}^{2n} W_i^{\text{cov}} \left[\chi_{k+1}(i) - \hat{\mathbf{x}}_{k+1}^- \right] \left[\gamma_{k+1}(i) - \hat{\mathbf{y}}_{k+1}^- \right]^T$$
 (15b)

The innovation is defined as:

$$e_{k+1}^- \equiv \tilde{y}_{k+1} - \hat{y}_{k+1}^- \tag{16}$$

where \hat{y}_{k+1}^- is the weighted sum of all of the predicted measurements for each sigma point:

$$\hat{\mathbf{y}}_{k+1}^{-} = \sum_{i=0}^{2n} W_i^{\text{mean}} \gamma_{k+1}(i)$$
 (17)

The innovation covariance is the total output uncertainty due to state and measurement uncertainty:

$$P_{k+1}^{e_y e_y} = P_{k+1}^{yy} + R_{k+1} \tag{18}$$

The gain is then computed as:

$$K_{k+1} = P_{k+1}^{xy} (P_{k+1}^{e_y e_y})^{-1}$$
(19)

The estimated state and covariance updates are given by:

$$\hat{\mathbf{x}}_{k+1}^+ = \hat{\mathbf{x}}_{k+1}^- + K_{k+1} e_{k+1}^- \tag{20a}$$

Table 1
Chaser, target, and tether parameters.

Parameter	Value
Chaser inertia matrix J_C (kg-m ²)	diag(83.3, 83.3, 83.3)
Target inertia matrix J_T (kg-m ²)	diag(15 000, 3000, 15 000)
Chaser mass m_C (kg)	500
Target mass m_T (kg)	3000
Tether Young's modulus E (Pa)	60×10^9
Tether diameter d (m)	0.001
Tether natural length l_0 (m)	30
Tether damping c (N s/m)	16
Tether attachment point, chaser ${}^{C}\mathbf{r}_{tp,C}$ (m)	$[0.5, 0, 0]^T$
Tether attachment point, target ${}^{\tau}r_{tp,T}$ (m)	$[0, 0.875, 0]^T$
Secondary landmark ${}^{\tau}\boldsymbol{r}_L$ (m)	$[-0.6490, -1.1812, 0.7585]^T$

Table 2
Initial conditions.

Variable	Value
Chaser position R_C (km)	$[-6.176, -0.4207, 2.973]^T \times 10^3$
Target position R_T (km)	$[-6.176, -0.4208, 2.973]^T \times 10^3$
Chaser velocity V_C (km/s)	$[-2.45779, -4.40429, -5.71241]^T$
Target velocity V_T (km/s)	$[-2.45776, -4.40428, -5.71242]^T$
Chaser attitude quaternion q_C (–)	$[-0.5564, 0.6637, 0.4699, 0.1708]^T$
Target attitude quaternion q_T (–)	$[0.3214, -0.3830, 0.8138, 0.2962]^T$
Chaser angular velocity ω_C (rad/s)	$[0,0,0]^T$
Target angular velocity ω_T (rad/s)	$[0, -0.05, 0]^T$

$$P_{k+1}^{+} = P_{k+1}^{-} K_{k+1} P_{k+1}^{e_{y}e_{y}} K_{k+1}^{T}$$
(20b)

A full derivation of the UKF can be found in Ref. [33] or Ref. [34].

4. Simulation and results for symmetric target, centered tether attachment point

4.1. System simulation and measurement generation

As actual data does not yet exist for this problem, synthetic data needs to be created through simulation. The full dynamics and control of the chaser-tether-target system are simulated in MATLAB to gather the required data for estimation (see Bourabah et al. [32]). The tension magnitude is saved and corrupted with noise to simulate tether tension measurements, whereas the chaser's and target's orbital positions, the chaser's attitude quaternion, and the chaser and target tether attachment points in their respective body frames are saved to generate tracking measurements, as per Section 3.

During simulation, the chaser attitude is controlled through sliding mode control such that the x-axis of the chaser always points in the tether direction [32]. Additionally, proportional-integral-derivative (PID) control is implemented to determine thrust on the chaser that allows to achieve and then maintain a desired elongation in the tether throughout the simulation [32], to ensure tension and prevent whiplash effects and possible collisions (that were observed, for example, in [36] for bang-bang control). The PID control determines the thrust force on the chaser along the tether unit vector, and the control law is given by: $F = K_P e + K_I \int_0^t e \, dt + K_D \dot{e}$. The proportional, integral, and derivative gains are chosen to be $K_P = 300 \text{ kg/s}^2$, $K_I = 300 \text{ kg/s}^3$, and $K_D = 2000 \text{ kg/s}$, respectively, and e is given by $e = \delta l + l_0 - l$, where δl is the desired elongation. The chaser, tether, and target parameters for the simulated system are presented in Table 1. With the parameters in the table, the tether's spring constant can be calculated as k = 1 $E\pi(d/2)^2/(l_0)$. The initial conditions to simulate the entire system are provided in Table 2. An initial tether elongation of $(l - l_0) = -1$ m is selected, such that the tether is initially slack by 1 m.

As discussed in Section 2, the gravity gradient torque on the target is neglected in this work. To verify that such an assumption is reasonable, the magnitude of the gravity gradient torque that would be experienced by the target is compared to the magnitude of the torque generated by

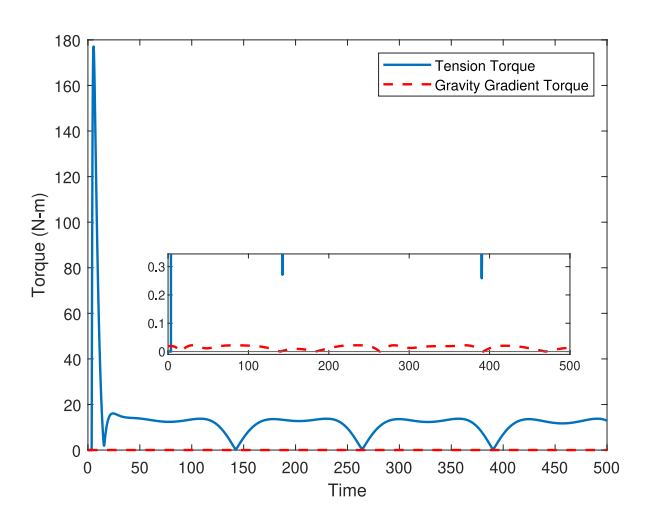


Fig. 3. Torques created by the tension and by the gravity gradient on the target.

tension on the debris in Fig. 3. The gravity gradient torque is evaluated as [37]:

$$\boldsymbol{\tau}_{g}(t) = \frac{3\mu_{e}}{\left\|\boldsymbol{\mathcal{T}}\boldsymbol{R}_{T}(t)\right\|^{5}} S(\boldsymbol{\mathcal{T}}\boldsymbol{R}_{T}(t)) J(\boldsymbol{\mathcal{T}}\boldsymbol{R}_{T}(t)) \tag{21}$$

where μ_e is the standard gravitational parameter for Earth and ${}^{\mathcal{T}}\mathbf{R}_T(t)$ denotes the inertial position of the center of mass of the target, expressed in the target body frame. As is clear from the zoom in Fig. 3, the minimum torque generated by the tension in the tether (occurring at approx. 390 s) is more than 10 times the maximum torque generated by the gravity gradient. Therefore, this comparison confirms that the gravity gradient torque may be reasonably ignored.

The measurements are taken to be the tether tension and the pixel coordinates of 2 features being tracked on the target. To generate these measurements, the tension history and pixel coordinates of tracked features must be saved and injected with noise. The magnitude of the tension in the tether is saved at each time step throughout the simulation and corrupted with noise as per Eq. (11), where $h(x_k)$ represents the saved tension magnitude T and v_k is the simulated noise. On the other hand, the pixel coordinate measurements need to be created from the attitude information of the target. The features being tracked are first selected as the tether attachment point on the target and one additional feature with random target body-frame coordinates. As the tether attachment point is on the y-axis of the debris, a second feature that is not on the y-axis must be added to obtain moment information around all three axes, which is expected to be sufficient for estimation. These features are then processed through the pinhole projection model to generate pixel coordinate measurements, which are then corrupted by noise. The position of the secondary landmark selected in this work is provided (expressed in the target reference frame) in Table 1 as ${}^{\tau}r_{I}$.

Tension measurements are based on the TE-RFS tension sensor,² where the noise added to the true tension measurements is taken to have a Gaussian distribution with 0 mean and a standard deviation of 10 N. An example of the generated tension magnitude measurements can be seen in Fig. 4, where the blue line represents the measured tension value and the black line is the true simulated tension magnitude. In cases where the measured tension is negative, the measurement is taken to be 0 N. It can be seen that the control implemented for the simulation maintains a true tension magnitude of approx. 15 N after undergoing a brief spike of approx. 420 N. This behavior is caused by

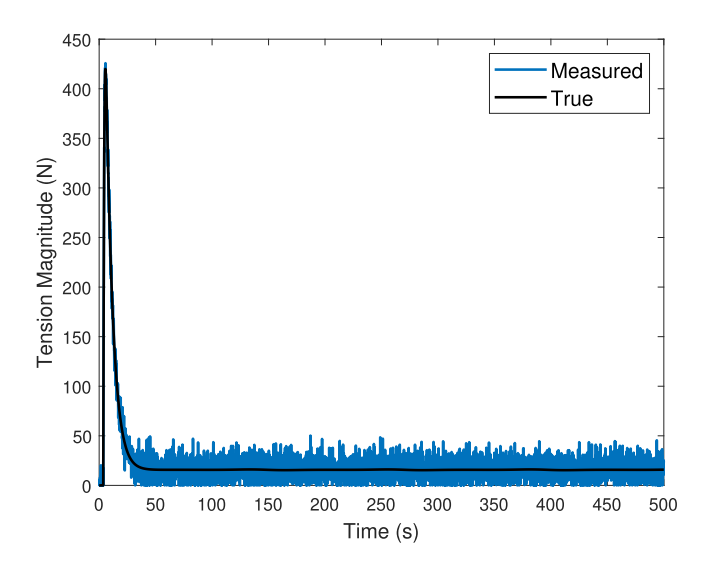


Fig. 4. True and measured tension magnitude. (For interpretation of the references to color in this figure legend, the reader is referred to the web version of this article.)

the tether being initially slack and confirms the proper operation of the PID controller. As the tether remains taut after an initial spike, a moment force is continuously applied to the target debris, which can therefore be used for the estimation of the principal moments of inertia of the debris.

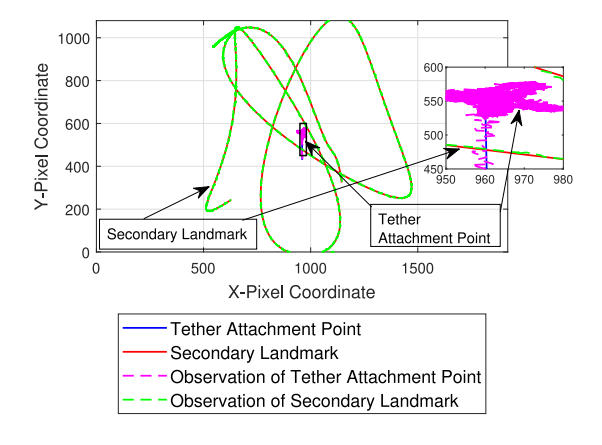
The pinhole camera frame is centered on the chaser spacecraft. The model of the pinhole camera depends on the focal length, sensor size, sensor resolution, and the principal point offset, and is built as per Eqs. (13)–(14), which represent $h(x_k)$. As with tension, noise is added according to v_k when generating the actual measurement. A longer focal length produces a narrower field of view (FOV), while a larger sensor size produces a wider FOV. For this work, the focal length is set to f=80 mm, the sensor size is taken to be $20 \text{ mm} \times 11.25 \text{ mm}$, and the resolution is assumed to be 1920×1080 pixels. The scales between the image space and world space can be calculated by dividing the resolution by the sensor size (i.e., $s_{x'}=1920/20$ pixels/mm and $s_{y'}=1080/11.25$ pixels/mm). For our purposes, it is also assumed that the principal point offset is zero, meaning that the camera bore sight goes through the exact center of the image (i.e., $c_{x'}=960$ pixels and $c_{y'}=540$ pixels).

Fig. 5(a) shows a time history of the projections of the tether attachment point and of the secondary tracked point through this camera model. The solid blue and dashed pink lines denote the projections of the true and measured pixel position of the tether attachment point on the camera sensor, respectively. The solid red and dashed green lines show the true and measured position of the secondary landmark, respectively. For both the tether attachment point and the secondary landmark, the measured pixel coordinates overlap the true pixel coordinates closely, but are distinct from the latter — as can be seen from the zoomed section. Fig. 5(b) shows the corresponding noise over time, which has a standard deviation of 2 pixels. Important to notice from Fig. 5(a) is also that there are two periods in which the secondary landmark exits the camera FOV, with the shorter period occurring between 230 s and 240 s into the simulation, and the longer period occurring between 270 s and 370 s into the simulation. The effect of these will be discussed in the next Section.

4.2. Estimation performance

In this Section, the performance of the UKF in estimating the principal moments of inertia, angular velocity, and attitude error of the target debris is evaluated by means of Monte-Carlo simulations. It should be recalled that estimation is achieved under the following assumptions: (1) The relative position of the target with respect to the

² TE-RFS Multi-Configuration Tension Sensor. https://www.checkline.com/tension_sensors/te-rfs. Last accessed 24 Feb. 2023.



a Tracked feature observations.

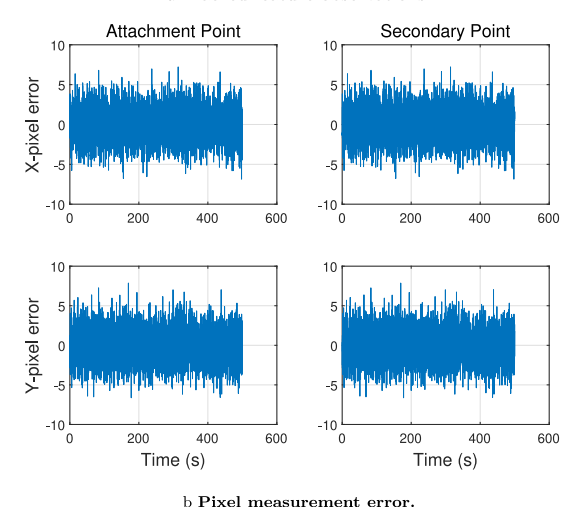


Fig. 5. Time history of pixel-coordinate measurements of tracked debris features. (For interpretation of the references to color in this figure legend, the reader is referred to the web version of this article.)

chaser is known while the attitude and angular rates of the target are estimated. (2) The tension magnitude in the tether is measured, and the tether attachment point and secondary landmark on the target body in the target body frame are known. (3) The attitude, angular velocity, and tether attachment point on the chaser craft, as well as the tether properties, are assumed to be known. (4) Views of the secondary landmark and of the tether attachment point are never blocked by the geometry of the target. (5) The tension and pixel coordinate measurements are made available every 0.1 s.

Once the required data and measurements are created, the UKF is initialized with a variance-covariance matrix of $P = diag((1 \times 1)^{-1})$ 10^{-2} (rad)^2 , $(1 \times 10^{-2} \text{ (rad)})^2$, $(1 \times 10^{-2} \text{ (rad)})^2$, $(1 \times 10^{-2} \text{ (rad/s)})^2$, $(1 \times 10^{-2} \text{ (rad/s)})^2$ $10^{-2} (rad/s)^2$, $(1 \times 10^{-2} (rad/s))^2$, $(1250 (kg-m^2))^2$, $(250 (kg-m^2))^2$, $(1250 (kg-m^2))^2$ (kg-m²))²) where the first three components are the initial uncertainties in the Euler angles, the central three components (i.e., elements 4, 5, and 6) are the initial uncertainties in the angular rates, and the last three components are the initial uncertainties in the principal moments of inertia. The initially estimated target attitude quaternion is taken to be the true attitude of the debris. The initial Euler angle errors, angular rates, and moment of inertia estimates are generated randomly at the start of each Monte-Carlo run. The Euler angle errors are generated using a normal distribution with a standard deviation of 1×10^{-2} (rad), while the angular rates are perturbed from the true initial angular rate with a standard deviation of 1×10^{-2} (rad/s). The initial moment of inertia is assumed to be known within 25% of the true value at the start of each Monte-Carlo run. The process noise matrix is taken to be $Q = \text{diag}(1 \times 10^{-32} \text{ (rad)}, 1 \times 10^{-32} \text{ (rad)}, 1 \times 10^{-32} \text{ (rad)}, 3 \times 10^{-8} \text{ (rad/s)},$

 3×10^{-8} (rad/s), 3×10^{-8} (rad/s), 0 (kg-m²), 0 (kg-m²), 0 (kg-m²)), where the higher process noise for the angular rates is due to the uncertainty in the tension measurements. As the moments of inertia of the target are assumed to remain constant, there is no process noise in the dynamics of these parameters. Moreover, there are no disturbance sources affecting the debris, making the process noise for the attitude dynamics small. The tunable parameters α , β , and κ are set to 0.0001, 14, and 14, respectively. The pixel coordinate measurements are corrupted by noise with a variance of 4 pixels, making the measurement covariance matrix R = diag(4, 4, 4, 4).

The time histories of the errors and their respective bounds for a single (randomly selected) run of the Monte-Carlo simulation are presented in Figs. 6–8, along with the actual distribution of the estimation errors across all runs. In particular, blue lines represent errors for this particular run, and the solid black lines show the 3- σ bound provided by the UKF. The green, yellow, and red zones show the areas between the 1-, 2-, and 3- σ bounds of the entire Monte-Carlo simulation, respectively.

The Euler angle error history is presented in Fig. 6. As can be seen, the attitude error remains within 1° during the majority of the simulation, with the exception of the pitch estimate between approx. 270 s and 370 s. As previously mentioned, during this time the secondary

 $^{^3}$ The tunable parameters were selected based on a particle swarm optimization in which the mean error was minimized across 10 runs of the Monte Carlo simulation.

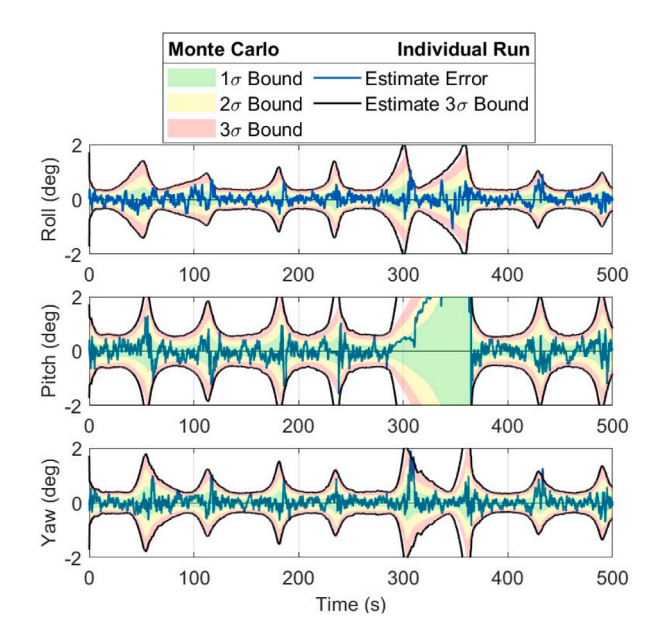


Fig. 6. Error in the estimated attitude of target debris. (For interpretation of the references to color in this figure legend, the reader is referred to the web version of this article.)

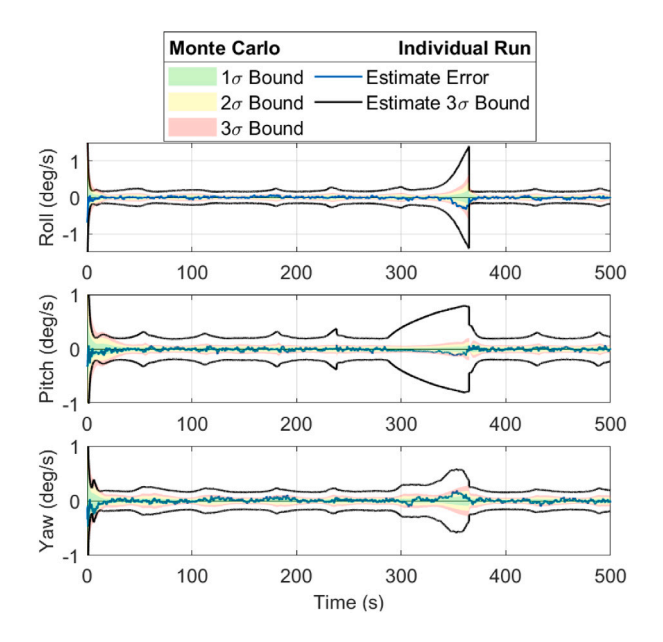


Fig. 7. Error in the estimated angular rates of target debris. (For interpretation of the references to color in this figure legend, the reader is referred to the web version of this article.)

feature being tracked exits the camera FOV. The only visible feature during this time is the tether attachment point, which cannot provide information on the torque about the *y*-axis of the debris; as a result, the pitch estimate rapidly degrades, while the roll and yaw estimates only degrade slightly. Although the actual errors often remain within 1°, the Monte Carlo 3- σ bounds extend to approx. 2° at times for the roll and yaw axes, and to approx. 21° for the pitch axis (with an estimated bound of 31° for the individual run between 280 s and 380 s). It can also be noticed that the individual run's 3- σ bounds closely match the 3- σ bounds of the Monte-Carlo simulation results, suggesting that the filter appropriately estimates the Euler angle error distribution.

The angular rate errors are presented in Fig. 7. Similar to the time history of the Euler angle error estimates, a brief period of greater uncertainty in the estimates produced by the UKF is visible between approx. 270 s and 370 s. In fact, the re-appearance of the secondary

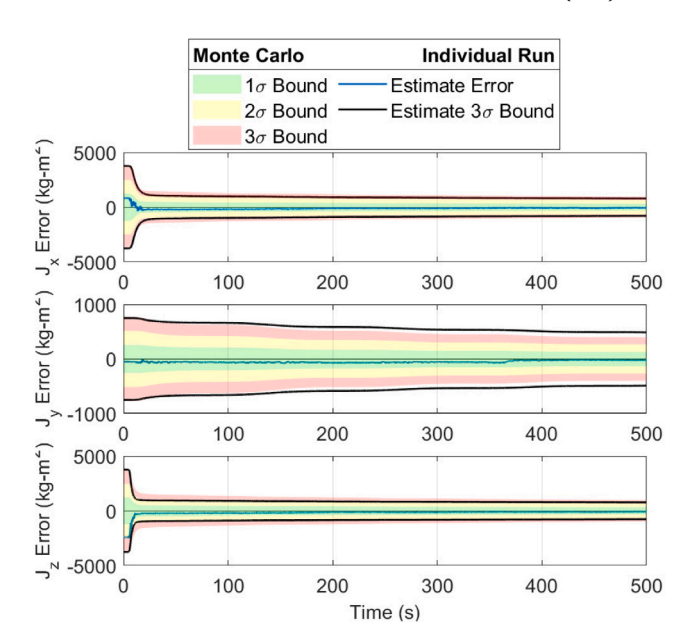


Fig. 8. Error in estimated target debris principal moments of inertia. (For interpretation of the references to color in this figure legend, the reader is referred to the web version of this article.)

feature in the camera FOV is characterized by a noticeable decrease in the $3\text{-}\sigma$ bound at approx. 370 s. Unlike the Euler angle error estimates, the $3\text{-}\sigma$ bounds calculated by the UKF for this run are approx. twice as large as the Monte-Carlo $3\text{-}\sigma$ bounds of approx. 0.13 deg/s. Despite these larger predicted bounds, the actual estimated angular rates distribution remains within 0.1 deg/s of the true angular rates of the target, which is within the Monte-Carlo $3\text{-}\sigma$ bounds. It is clear that the UKF is too conservative with its angular rate estimates. As the Monte-Carlo distributions of the estimated angular rates are significantly smaller than the predicted distribution, the predictions made by the UKF for the angular rates are actually precise and accurate when both tracked features appear in the camera FOV.

The principal moments of inertia estimates provided by the UKF during this particular run are presented in Fig. 8. In contrast to the attitude and angular rate error plots, the $3-\sigma$ bounds of the moment of inertia estimates do not undergo a series of increases and decreases in uncertainty and are not affected by the secondary feature exiting the FOV of the camera. In fact, for both the moments of inertia about the x- and z-axes, the bounds remain large for a short time, before quickly converging around 6 s into the simulation. After the initial rapid convergence, the bounds gradually continue converging until the end of the simulation. The rapid convergence in the bounds occurs approx. at the same time as the initial spike in tension caused by the initial slackness in the tether (as demonstrated in Fig. 4). Unlike what is observed for J_x and J_z , the bounds of the estimated principal moment of inertia errors about the y-axis decrease gradually throughout the simulation, rather than having a period of rapid convergence. Moreover, the bounds provided by the UKF for this run predict a smaller distribution for the moments of inertia about the x- and z-axes, whereas the moment of inertia about the y-axis has a greater predicted distribution compared to the Monte-Carlo distribution.

Similar trends can be appreciated for the errors in the estimates of the moments of inertia (see the blue lines). Despite the moments of inertia about the *x*- and *z*-axes being characterized by a large

 $^{^4}$ Conservative estimates are caused by the selected process noise Q. Angular rate components were intentionally raised due to uncertainty in the effects of tension measurement noise on the propagation of the states. Reducing these components would improve the uncertainty bounds, at the risk of making the filter over-confident and possibly converging toward an incorrect estimate.

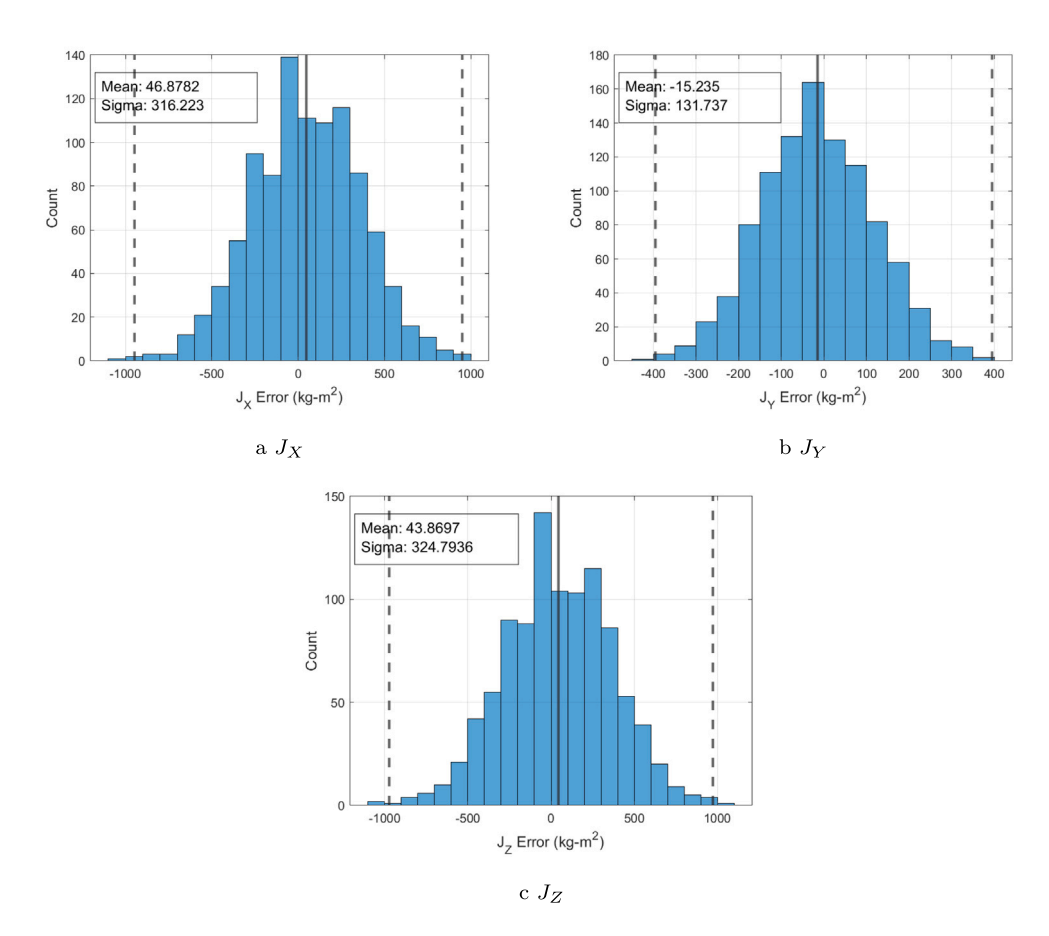


Fig. 9. Final principal moments of inertia estimate error distributions.

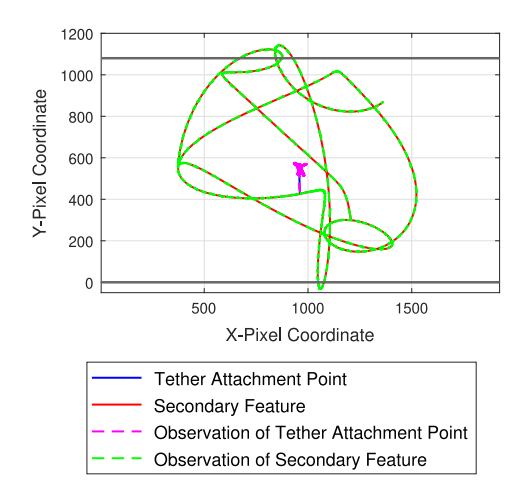


Fig. 10. Tracked feature observations for the non-symmetric case.

initial error, the filter is capable of rapidly converging toward the true moments of inertia, with the majority of the convergence occurring around 6 s. In fact, from 5 s to 20 s, the estimate errors for J_x and J_z change by approx. 600 kg-m² and approx. 2300 kg-m², respectively. After this initial convergence, the error between the true and estimated moments of inertia about the x- and z-axes change by approx. 150 kg-m² between 20 s and 500 s. On the other hand, the moment of inertia about the y-axis undergoes the majority of its convergence between 360 s and 380 s, when the error changes by approx. 50 kg-m²; afterward, the error remains roughly constant until the end of the simulation.

For statistical analysis, the distributions of the errors of the final moments of inertia estimates made by the UKF across all 1000 runs of

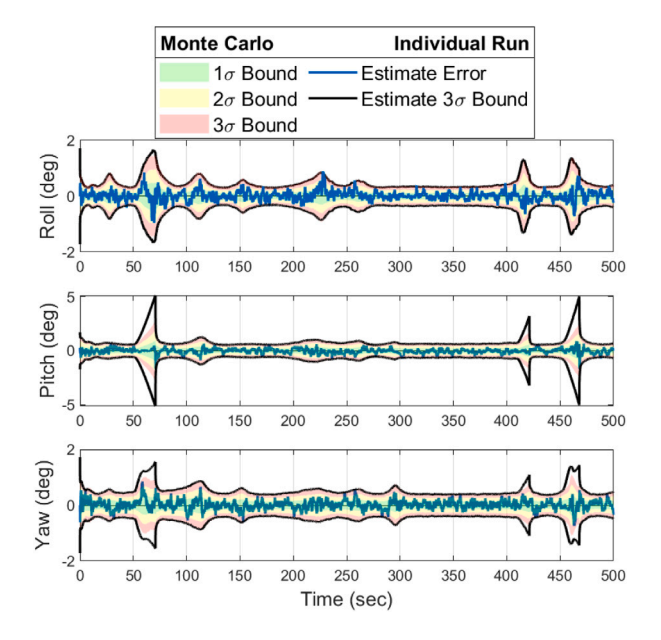


Fig. 11. Error in the estimated attitude of non-symmetric target.

the Monte Carlo simulation are presented in Fig. 9. Each bin separates the final estimate errors every 100 kg-m² for the J_x and J_z final error distribution plots, and every 50 kg-m² for the J_y final error distribution plot. The solid black lines show the average final estimate errors, whereas the dashed lines show the 3- σ bounds of the final estimate errors. The text box provides values for the mean estimate error along with the 1- σ value of the estimate errors. It is evident that the average

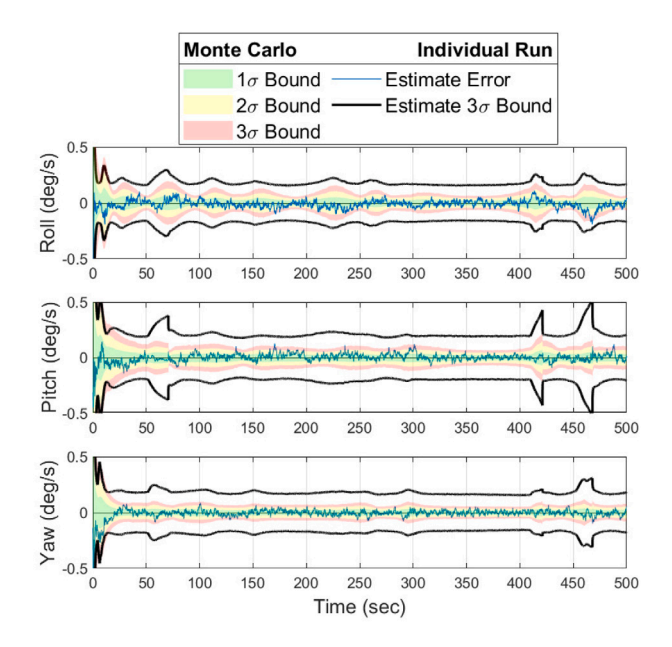


Fig. 12. Error in the estimated angular rates of non-symmetric target.

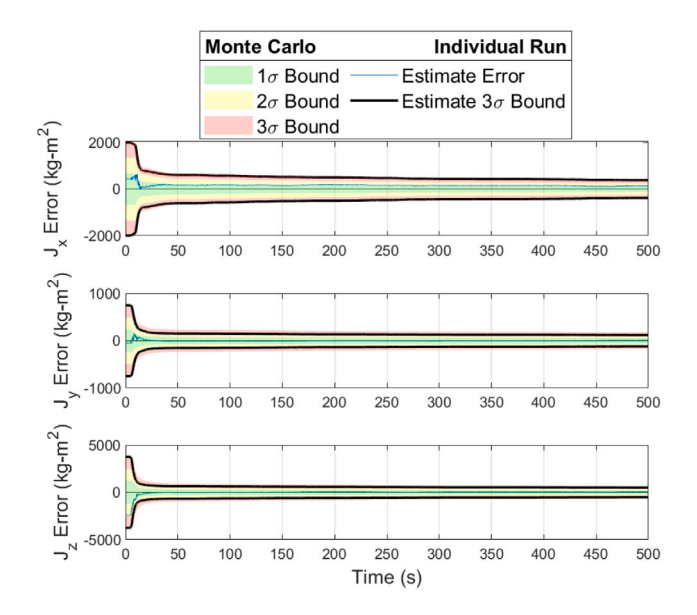


Fig. 13. Error in the estimated principal moments of inertia of non-symmetric target.

final errors for all the moments of inertia are within 50 kg-m², which is 0.33% of the true moments of inertia about the x- and z-axes and 1.66% of the true moment of inertia about the y-axis. When accounting for the 3- σ bounds, 99.7% of the final moment of inertia estimates will be within 6.64%, 13.68%, and 6.79% of the true values of the moments of inertia about the x-, y-, and z-axes, respectively. These J_x and J_z estimates are approx. 5% worse, and the J_y estimates are approx. 10% worse than the estimates in previous work [32]; however, this is due to the fact that previous work assumed perfect knowledge of tether tension and the availability of angular rate measurements, which are more ideal conditions.

In all cases, it can be noted that the largest bin of estimate errors is the first to the left of the zero-error point, signifying that the filter is more likely to estimate a slightly lower moment of inertia than the true value, within 100 kg-m^2 for the x- and z-axes, and within 50 kg-m^2 for the y-axis. While the final moment of inertia estimate errors about the y-axis across all runs follow a normal distribution with a slight skew, the final moment of inertia estimate errors about the x- and z-axes follow

a more bimodal distribution curve, in which a larger peak in estimate errors falls within the 0 to -100 kg-m^2 range, and a smaller second peak appears in the 200 to 300 kg-m² range.

Overall, these results demonstrate that the implemented UKF is capable of obtaining estimates of the principal moments of inertia of the target debris given pixel coordinates of two tracked landmarks and measurements of the tension in the tether. Nearly all the estimates are within 7% of the moments of inertia about the x- and z- axes, after a brief period of tension measurements. However, it was also demonstrated that it is most likely that the UKF will estimate the principal moments of inertia to within 2% of the true value. Under the assumptions of this work, the UKF is also capable of estimating the attitude of the target within 2°, unless a tracked feature exits the camera FOV. Finally, the angular rates of the target can be estimated accurately, to within 0.2 deg/s, despite a significantly lower confidence in its estimates.

5. Estimation results for non-symmetric target, non-centered tether attachment point

Although it was shown in Section 4 that the filter can estimate the principal moments of inertia of a tethered target in the case of a symmetric object with a tether attached along one of its principal axes, these specific conditions may not necessarily occur. The estimation performance is therefore evaluated here in a non-symmetric case, in which the principal moments of inertia matrix of the target is $J_T = \text{diag}(8000, 3000, 15\,000) \text{ kg-m}^2$ and the position of the tether attachment point on the target is ${}^{\tau}r_{tp,T} = [-0.1, 0.875, -0.25]^T$ m. All other parameters are assumed to be the same as in Tables 1 and 2.

The time history of the projections of the tracked features through the camera model is presented in Fig. 10. The horizontal black lines represent the limits of the camera frame (i.e., 0 and 1080 pixels) so that the position of the tracked features when not in the camera frame may be seen by the reader; as before, measurements are ignored any time the tracked features are not in the FOV of the camera. Differently from the symmetric case, there are now three periods in which the secondary point leaves the FOV of the camera, but of shorter duration, occurring between 52 s and 71 s, between 410 s and 421 s, and between 453 s and 468 s.

The estimation performance for each of the states can be appreciated in Figs. 11–13. As in the symmetric case, the attitude estimate errors (see Fig. 11) often remain within 1° of the true value, and their Monte-Carlo distribution remains within 2°. Again, when the secondary feature is not visible to the camera, the uncertainty rapidly grows (which occurs three times as expected); however, it is contained at 5°. The lower values of the uncertainties, compared to what was observed in Section 4, are attributed to the shorter periods of time in which the secondary feature is lost and therefore – ultimately – to the dynamics of the target object.

The angular rate estimation results for the non-symmetric case are shown in Fig. 12. Again, the $3-\sigma$ bounds of the individual run are larger than the Monte-Carlo $3-\sigma$ bounds, indicating that the filter is not as confident as it could be. Moreover, the average uncertainty bound remained similar in the two cases, with a $3-\sigma$ bound of approx. $0.18^{\circ}/s$. The angular rate estimates in this case, however, are characterized by uncertainties that do not vary much in case of loss of a tracked feature.

The greatest difference with respect to the symmetric target case can be found in the J_y estimate (see the central plot in Fig. 13), which now converges in approx. 20 s, with a similar trend to J_x and J_y . This result suggests that the torque applied to the target through the noncentered tether is now sufficient to estimate all three principal moments of inertia. It is also confirmed from Fig. 13 that the loss of tracked features does not affect the principal moment of inertia estimation directly.

A statistical analysis of the distribution of the final principal moment of inertia estimates across the entire Monte-Carlo simulation is

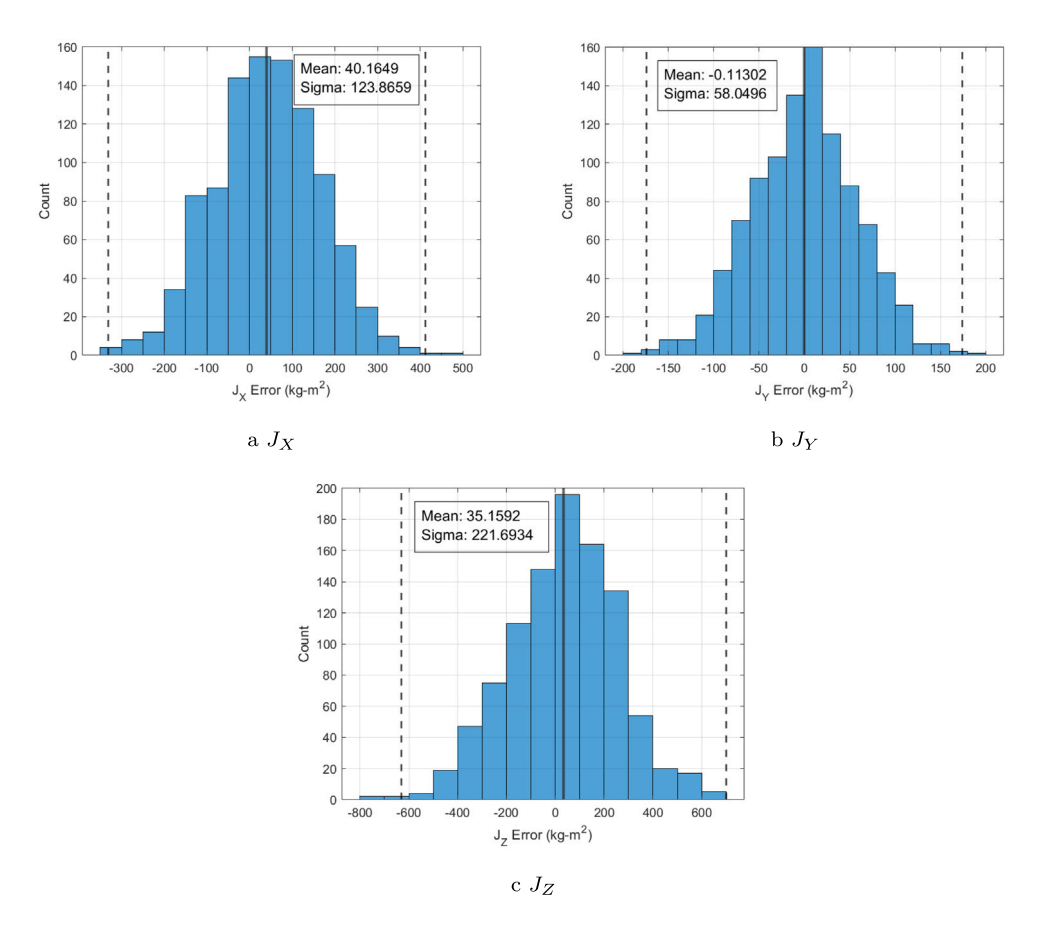


Fig. 14. Final principal moments of inertia estimate error distributions for the non-symmetric case.

presented in Fig. 14. The average estimate for J_y is now observed to be nearly perfect; when taking into account the standard deviation of the final estimates across the Monte-Carlo simulation, the filter will predict J_y within 5.81% of the true value. As far as J_x and J_z are concerned, the average estimates do not vary significantly from the symmetric case (decreasing by only approx. 10 kg-m²); on the other hand, the standard deviations decrease by approx. 200 kg-m² and 100 kg-m², respectively, making the filter more precise. In this case, J_x and J_z are estimated within 5.15% and 4.67% of their true values.

Overall, it can be concluded that in the case of a non-symmetric target and non-centered tether attachment point, the filter can estimate the principal moments of inertia accurately and precisely, and even show improvements compared to the symmetric case. The greatest improvement was observed in the accuracy of the J_y estimate, while accuracy remained approximately unchanged for J_x and J_z ; precision increased for all the principal moments of inertia estimates. The attitude and angular rate estimates improved only slightly, and this was found to be due to the different rotational motion of the target in this scenario, which caused shorter periods of tracked feature loss.

6. Conclusion

Estimation of the principal moments of inertia of tethered space debris, based on tracking of two features on the target and tension measurements, was investigated in this paper. Synthetic data was generated through simulation of the dynamics of a chaser–tether–target system including chaser attitude control and relative distance-based tension control. A UKF was employed for estimation, in its standard formulation for angular rates and mass moments of inertia, and in the USQUE formulation for attitude. Symmetric and non-symmetric capture cases were investigated.

Utilizing the target attitude estimates and the tension measurements, the tension vector can be recreated and used to calculate the moment applied to the target. With this information available, the moments of inertia can be estimated well by the UKF, irrespective of possible temporary loss of a tracked feature, in both cases. It was further shown that estimation of the principal moments of inertia may benefit from a non-symmetric target or non-centered attachment. Accurate and precise estimates of the attitude and angular rates of the target debris were found throughout most of the dynamics, although in the event that a tracked feature exits the camera FOV, accuracy and precision drop dramatically until view of that feature is restored. As a result, this work demonstrated that the attitude, angular rates, and moments of inertia of tethered debris can be successfully estimated by a UKF using tension and pixel-coordinate measurements of two tracked landmarks.

Declaration of competing interest

The authors declare that they have no known competing financial interests or personal relationships that could have appeared to influence the work reported in this paper.

Acknowledgments

This work was funded by the National Science Foundation (NSF), under the CMMI Program, Award number 2105011. Derek Bourabah also acknowledges reception of the NASA Space Grant Fellowship. Chris Gnam also acknowledges reception of the National Science Foundation's Graduate Research Fellowship, which helped to support his contribution to this work under Grant No. 2020305048.

References

- R. Miller, Orbital debris quarterly news-volume 25, issue 4, Orbit. Debris Q. News 25 (4) (2021).
- [2] J.C. Liou, An active debris removal parametric study for LEO environment remediation, Adv. Space Res. 47 (11) (2011) 1865–1876, http://dx.doi.org/10. 1016/j.asr.2011.02.003.
- [3] J.C. Liou, N.L. Johnson, N.M. Hill, Controlling the growth of future LEO debris populations with active debris removal, Acta Astronaut. 66 (5–6) (2010) 648–653, http://dx.doi.org/10.1016/j.actaastro.2009.08.005.
- [4] B. Bischof, ROGER-robotic geostationary orbit restorer, in: 54th International Astronautical Congress of the International Astronautical Federation, the International Academy of Astronautics, and the International Institute of Space Law, Bremen, Germany, 2003, http://dx.doi.org/10.2514/6.IAC-03-IAA.5.2.08, IAA-5.
- [5] K. Wormnes, J.H. de Jong, H. Krag, G. Visentin, Throw-nets and tethers for robust space debris capture, in: Proceedings of the 64th International Astronautical Congress, Beijing, China, 2013, IAC-13, A6.5, 2x16445.
- [6] M. Lavagna, V. Pesce, R. Bevilacqua, Uncooperative objects pose, motion and inertia tensor estimation via stereovision, in: Advanced Space Technologies for Robotics and Automation 2015, Noordwijk, Netherlands, 2015.
- [7] F. Zhang, P. Huang, Releasing dynamics and stability control of maneuverable tethered space net, IEEE/ASME Trans. Mechatronics 22 (2) (2016) 983–993, http://dx.doi.org/10.1109/TMECH.2016.2628052.
- [8] E.M. Botta, C. Miles, I. Sharf, Simulation and tension control of a tether-actuated closing mechanism for net-based capture of space debris, Acta Astronaut. 174 (2020) 347–358, http://dx.doi.org/10.1016/j.actaastro.2020.04.052.
- [9] V.S. Aslanov, V.V. Yudintsev, Behavior of tethered debris with flexible appendages, Acta Astronaut. 104 (1) (2014) 91–98, http://dx.doi.org/10.1016/j.actaastro.2014.07.028.
- [10] R. Dudziak, S. Tuttle, S. Barraclough, Harpoon technology development for the active removal of space debris, Adv. Space Res. 56 (3) (2015) 509–527, http://dx.doi.org/10.1016/j.asr.2015.04.012.
- [11] G.S. Aglietti, B. Taylor, S. Fellowes, S. Ainley, D. Tye, C. Cox, A. Zarkesh, A. Mafficini, N. Vinkoff, K. Bashford, T. Salmon, I. Retat, C. Burgess, A. Hall, T. Chabot, K. Kanani, A. Pisseloup, C. Bernal, F. Chaumette, A. Pollini, W.H. Steyn, RemoveDEBRIS: An in-orbit demonstration of technologies for the removal of space debris, Aeronaut. J. 124 (1271) (2019) 1–23, http://dx.doi.org/10.1017/aer.2019.136.
- [12] V.S. Aslanov, Chaos behavior of space debris during tethered tow, J. Guid. Control Dyn. 39 (10) (2016) 2399–2405, http://dx.doi.org/10.2514/1.G001460.
- [13] V.S. Aslanov, V.V. Yudintsev, Chaos in tethered tug-debris system induced by attitude oscillations of debris, J. Guid. Control Dyn. 42 (7) (2019) 1630–1637, http://dx.doi.org/10.2514/1.G004162.
- [14] R. Qi, A.K. Misra, Z. Zuo, Active debris removal using double-tethered space-tug system, J. Guid. Control Dyn. 40 (3) (2017) 722–730, http://dx.doi.org/10.2514/ 1.G000699.
- [15] V. Yudintsev, V. Aslanov, Detumbling space debris using modified yo-yo mechanism, J. Guid. Control Dyn. 40 (3) (2017) 714–721, http://dx.doi.org/10.2514/1.G000686.
- [16] B. Wang, Z. Meng, P. Huang, Attitude control of towed space debris using only tether, Acta Astronaut. 138 (2017) 152–167, http://dx.doi.org/10.1016/ i.actaastro.2017.05.012.
- [17] W.J. O'Connor, D.J. Hayden, Detumbling of space debris by a net and elastic tether, J. Guid. Control Dyn. 40 (7) (2017) 1832–1836, http://dx.doi.org/10. 2514/1.G001838.
- [18] M. Shan, L. Shi, Post-capture control of a tumbling space debris via tether tension, Acta Astronaut. 180 (2021) 317–327, http://dx.doi.org/10.1016/j.actaastro. 2020.12.049
- [19] B.E. Tweddle, Computer Vision-Based Localization and Mapping of an Unknown, Uncooperative and Spinning Target for Spacecraft Proximity Operations (Ph.D. thesis), Massachusetts Institute of Technology, 2013.
- [20] B.E. Tweddle, A. Saenz-Otero, J.J. Leonard, D.W. Miller, Factor graph modeling of rigid-body dynamics for localization, mapping, and parameter estimation of a spinning object in space, J. Field Robotics 32 (6) (2015) 897–933, http: //dx.doi.org/10.1002/rob.21548.
- [21] S. Corpino, S. Mauro, S. Pastorelli, F. Stesina, G. Biondi, L. Franchi, T. Mohtar, Control of a noncooperative approach maneuver based on debris dynamics feedback, J. Guid. Control Dyn. 41 (2) (2018) 431–448, http://dx.doi.org/10. 2514/1.G002685.
- [22] M.D. Lichter, S. Dubowsky, State, shape, and parameter estimation of space objects from range images, in: IEEE International Conference on Robotics and Automation, Vol. 3, IEEE, 2004, pp. 2974–2979, http://dx.doi.org/10.1109/ ROBOT.2004.1307513.
- [23] Y. Murotsu, K. Senda, M. Ozaki, S. Tsujio, Parameter identification of unknown object handled by free-flying space robot, J. Guid. Control Dyn. 17 (3) (1994) 488–494, http://dx.doi.org/10.2514/3.21225.
- [24] O. Ma, H. Dang, K. Pham, On-orbit identification of inertia properties of spacecraft using a robotic arm, J. Guid. Control Dyn. 31 (6) (2008) 1761–1771, http://dx.doi.org/10.2514/1.35188.

- [25] T.C. Nguyen-Huynh, I. Sharf, Adaptive reactionless motion and parameter identification in postcapture of space debris, J. Guid. Control Dyn. 36 (2) (2013) 404–414, http://dx.doi.org/10.2514/1.57856.
- [26] T. Zhang, X. Yue, X. Ning, J. Yuan, Stabilization and parameter identification of tumbling space debris with bounded torque in postcapture, Acta Astronaut. 123 (2016) 301–309, http://dx.doi.org/10.1016/j.actaastro.2016.04.007.
- [27] J. Peng, W. Xu, E. Pan, L. Yan, B. Liang, A.-g. Wu, Dual-arm coordinated capturing of an unknown tumbling target based on efficient parameters estimation, Acta Astronaut. 162 (2019) 589–607, http://dx.doi.org/10.1016/j.actaastro.2019.03.
- [28] Z. Chu, Y. Ma, Y. Hou, F. Wang, Inertial parameter identification using contact force information for an unknown object captured by a space manipulator, Acta Astronaut. 131 (2017) 69–82, http://dx.doi.org/10.1016/j.actaastro.2016. 11 019
- [29] E. Netzer, T.R. Kane, Estimation and control of tethered satellite systems, J. Guid. Control Dyn. 18 (4) (1995) 851–858, http://dx.doi.org/10.2514/3.21469.
- [30] Q. Zhang, E.G. Asri, Z.H. Zhu, Space tether system state estimation using distributed fibre optical strain measurement, inverse finite element method and Kalman filter, Acta Astronaut. 211 (2023) 435–446, http://dx.doi.org/10.1016/ j.actaastro.2023.06.020.
- [31] F. Zhang, I. Sharf, A. Misra, P. Huang, On-line estimation of inertia parameters of space debris for its tether-assisted removal, Acta Astronaut. 107 (2015) 150–162, http://dx.doi.org/10.1016/j.actaastro.2014.11.016.
- [32] D. Bourabah, L. Field, E.M. Botta, Estimation of uncooperative space debris inertial parameters after tether capture, Acta Astronaut. 202 (2023) 909–926, http://dx.doi.org/10.1016/j.actaastro.2022.07.041.
- [33] J.L. Crassidis, F.L. Markley, Unscented filtering for spacecraft attitude estimation, J. Guid. Control Dyn. 26 (4) (2003) 536–542, http://dx.doi.org/10.2514/2.5102.
- [34] J.L. Crassidis, F.L. Markley, Y. Cheng, Survey of nonlinear attitude estimation methods, J. Guid. Control Dyn. 30 (1) (2007) 12–28, http://dx.doi.org/10.2514/ 1.22452.
- [35] J.L. Crassidis, J.L. Junkins, Optimal Estimation of Dynamic Systems, first ed., 2004, pp. 312–314, http://dx.doi.org/10.1201/9780203509128.
- [36] L. Jasper, H. Schaub, Input shaped large thrust maneuver with a tethered debris object, Acta Astronaut. 96 (2014) 128–137, http://dx.doi.org/10.1016/ j.actaastro.2013.11.005.
- [37] P.C. Hughes, Spacecraft Attitude Dynamics, Dover Publications, Mineola, NY, 2004.



Derek Bourabah is a Ph.D. student in the Department of Mechanical and Aerospace Engineering at the University at Buffalo, NY. He holds a B.Sc. in Mechanical and Aerospace Engineering and an M.Sc. in Aerospace Engineering from the University at Buffalo as of 2021. His main research interests are in spacecraft dynamics and controls, and tethered satellite systems.



Chris Gnam is a Ph.D. student in the Department of Mechanical and Aerospace Engineering at the University at Buffalo, NY. He holds a B.A. in Mathematics with a minor in Physics, a B.Sc. in Aerospace Engineering, and an M.Sc. in Aerospace Engineering, and an M.Sc. in Aerospace Engineering from the University at Buffalo as of 2022. His main research interests are in spacecraft dynamics and navigation, as well as image rendering and image processing.



Dr. Eleonora M. Botta is an assistant professor in the Department of Mechanical and Aerospace Engineering at the University at Buffalo, NY. She holds a Ph.D. in Mechanical Engineering from McGill University, a B.Sc. in Aerospace Engineering and an M.Sc. in Space Engineering from Politecnico di Milano, and an M.Sc. in Aerospace Engineering from Politecnico di Torino. Her main research interests are the dynamics and control of tethered space systems, spacecraft trajectory optimization, and space situational awareness. She is a member of the AAS Space Flight Mechanics Committee and the vice-chair of the AIAA Space Tethers Technical Committee.